Cold start of polymer electrolyte fuel cells: Three-stage startup characterization

Yun Wang [a,*], Partha P. Mukherjee [b], Jeff Mishler [a], Rangachary Mukundan [b], Rodney L. Borup [b]

[a] Renewable Energy Resources Lab (RERL) and National Fuel Cell Research Center, Department of Mechanical and Aerospace Engineering, The University of California, Irvine, Irvine, CA 92697-3975, United States
[b] Los Alamos National Laboratory, Los Alamos, NM 87545, United States

ARTICLE INFO

ABSTRACT

In this paper, the electrochemical kinetics, oxygen transport and solid water formation within the cathode electrode of polymer electrolyte fuel cells (PEFCs) during cold start is investigated. We specifically evaluate the key parameters that govern the self-startup of PEFCs by considering a wide range of the relevant factors. These parameters include characteristic time scales of cell warm-up, ionomer hydration in the catalyst layer, ice build-up and melting, as well as the ratios of the time constants. Supporting experimental observation using neutron imaging and isothermal cold start experiment is discussed. Gas purge is found to facilitate the PEFC cold start but the improvement may be relatively small compared with other methods such as selecting suitable materials and modifying the cell design. We define a three-step electrode process for cold start and conduct a one-dimensional analysis, which enables the evaluation of the impact of ice volume fraction and temperature variations on the cell cold start performance. The ionic conductivity data of Nafion® 117 membrane at subfreezing temperature, evaluated from experiment, is utilized to analyze the temperature dependence of the ohmic polarization during cold start.

1. Introduction

The polymer electrolyte fuel cell (PEFC) is widely regarded as a potential power source for portable and mobile applications due to its noteworthy features of high efficiency and zero emission. PEFCs must have the ability to survive and start up from subfreezing temperatures, also called cold start, to be successfully deployed in automobiles. Under freezing environmental conditions, water produced has a tendency to freeze in open pores in the catalyst layer and GDL, rather than be removed from the fuel cell, thus creating mass transport limitations which eventually end the ability for operation.

Cold start is essentially a transient phenomenon. Currently, the majority of the efforts are focused on the steady-state characteristics of PEFCs. There is a lack of thorough investigation on the dynamic behavior, though the importance of dynamic characteristics is obvious for automobile and portable applications of fuel cells which are frequently subjected to fast load variations. While the characteristics of PEFC dynamics have been studied by several groups [1–11], research on PEFC cold start is relatively new [12–20]. Hishinuma et al. [12], Wilson et al. [13], McDonald et al. [14] and Cho et al. [15] conducted early studies on cold start. Hishinuma et al. [12] investigated cold start down to ∼−25 °C and found waste heat

generated by fuel cell might be sufficient to increase the PEFC temperature to 0 °C. Wilson et al. [13] investigated the impact of the freeze/thaw cycles on the electrode performance and concluded that freezing may not be detrimental to the integrity of the catalyst layer and membrane assembly. McDonald et al. [14] also conducted experiments to investigate the physical change in the electrolyte membrane due to freeze/thaw cycling. Cho et al. [15] carried out a study on cell degradation related to the thermal cycle and concluded that water freezing may be a source of cell degradation. Recently, Oszcipok et al. [16] examined the isothermal potentiostatic cold start and observed that water freezes in the cathode electrode, microporous layer, and the GDL. Yana et al. [17] investigated the impact of subfreezing temperatures on components and observed delamination of the catalyst layer during cold start. Mukundan et al. examined the fuel cell performance at subfreezing temperature and studied the influence of carbon paper and carbon cloth GDLs [18]. Wang [19] presented theoretical analyses of PEFC cold start operation and identified different stages during cold start. Refs. [20–23] proposed cold start models and examined the distributions of ice. Thompson et al. [24] investigated the isothermal operations at −20 °C.

Saito et al. [25] and Cappadonia et al. [26] investigated the membrane performance down to freezing temperatures. Saito et al. [25] investigated the ion and water transport in the membrane and concluded that part of the water is frozen around −20 °C, but nonfreezing water remains active for transport. Cappadonia et al. [26] measured the conductance of Nafion® membranes in a wide

* Corresponding author. Tel.: +1 949 824 6004; fax: +1 949 824 8585.
E-mail address: yunw@uci.edu (Y. Wang).

Nomenclature

A_m	electrode area (m²)
a	water activity; effective catalyst area per unit volume (m²/m³)
a_o	catalyst surface area per unit volume (m²/m³)
BP	bipolar plate
C	molar concentration of species k (mol/m³)
C_p	specific heat (J/kg K)
D	species diffusivity (m²/s)
EW	equivalent weight of dry membrane (kg/mol)
F	Faraday's constant (96,487 C/equivalent)
I	current density (A/cm²)
i	superficial current density (A/cm²)
j	transfer current density (A/cm³)
k	thermal conductivity (W/m K)
M	molecular weight (kg/mol)
P	pressure (Pa)
R	universal gas constant, 8.134 J/mol K; ohmic resistance (mΩ cm²)
S	source term
s_{ice}	ice volume fraction
t	time (s)
T	temperature (K)
U_o	equilibrium potential (V)

Greek symbols

α	transfer coefficient; net water flux per proton flux
ρ	density (kg/m³)
ϕ	phase potential (V)
σ	ionic conductivity (S/m)
λ	membrane water content, # of H_2O/SO_3H^- group
ε	porosity
η	surface overpotential (V)
τ	tortuosity/coverage coefficient; time constant (s)
δ	thickness (m)

Superscripts and subscripts

c	cathode
CL	catalyst layer
d	diffusion
e	electrolyte
eff	effective value
g	gas phase
m	membrane phase
o	reference value; initial value
ref	reference value
w	water

range of temperatures including the subzero regime. Song et al. [27] conducted a study on the oxygen reduction reaction (ORR) performance at subfreezing temperature and indicated that the ORR kinetics remains the same. Thompson et al. [28] investigated the ORR kinetics at subfreezing temperatures.

In view of the afore-mentioned approaches to cold start, theoretical analysis is highly desirable, particularly to identify and evaluate the key parameters governing the PEFC cold start operation. In our recent work [19], a theoretical framework was developed for PEFC cold start analysis. However, no extensive discussion has been made about the key parameters, particularly in the wide range of fuel cell properties that are considered in the literature. Building upon the theoretical framework [19], this paper defines three stages of cold start and presents a detailed analysis of the pertinent parameters, which are critical to the fundamental

understanding of the PEFC cold start operation. Observations from neutron imaging and isothermal cold start experiments are also provided along with the theoretical analysis. Further, this paper also discusses the temperature dependence of the ohmic polarization during cold start based on experimental data of Nafion® membrane ionic conductivity.

2. Simplified analysis and stages of cold start process

Fig. 1 schematically shows a PEFC and a high resolution TEM (transmission electron microscope) image of the catalyst layer [29]. A PEFC consists of many components that are essential for its proper functioning including: bipolar plate (BP), gas diffusion layer (GDL), catalyst layer (CL), and proton conducting membrane. The geometrical and physical parameters of these components are summarized in Table 1. At the electrochemical reaction surface in the cathode CL, oxygen reacts with protons and electrons from the hydrogen dissociation in the anode (see Fig. 1). Water and heat are the by-products of this reaction.

In the subzero environment, the above oxygen reduction reaction (ORR) is still active and able to produce water. Water production under subfreezing conditions has been observed indirectly by several experiments [12,14] (which show current production) and directly by neutron images, (see Fig. 2). Fig. 2 shows the evolution of the average water content under the channel and land, respectively, obtained from the neutron images. The neutron imaging was conducted at the NIST Center for Neutron Research (NCNR) on the thermal beam tube 2. The measurements were conducted using beam #1 and aperture #4 with a fluence rate of 2×10^7 neutrons/(cm² s). The fuel cell operates at subfreezing temperature of −10 and −20 °C, respectively, therefore the water will exist in solid state. It can be seen that the water content increases steadily with time due to the water production by the ORR. At subfreezing temperature, water freezing in the pores of the catalyst layer blocks the open pores required for reactant diffusion. To avoid cold start failure, the fuel cell needs to be heated by either external sources or self-heating, to at least 0 °C before ice in the catalyst layer causes severe reactant starvation.

2.1. Heat transfer in the cathode

The majority of heat is generated in the cathode catalyst layer primarily due to the large overpotential present at the reaction interface [30,31]. In a single PEFC, assuming all the waste heat is generated in the cathode catalyst layer, the upper limit of temperature variation across the catalyst layer can be estimated by considering a uniform heat generation removed via heat conduction [19]:

$$\Delta T_{CL} \sim \frac{\delta_{CL} I (E_o - V_{cell})}{2 k_{CL}^{eff}} \tag{1}$$

Note that the above equation considers a volumetric heat generation distributed within the catalyst layer, therefore the right side in the above is half of the one used in Ref. [19] where heat generation is treated as a surface flux added to the catalyst layer. The range of the effective thermal conductivity, k^{eff}, considered is from ∼0.3 to 3.0 W/m K. The typical thickness of the catalyst layer in PEFCs is varied from 7.5 to 25 μm. For standard cold start operation, i.e. 0.5 V and 0.1 A/cm², ΔT_{CL} ranges from 0.001 to 0.03 K, (which is negligible comparing with the overall temperature change during cold start).

The most common GDL materials are the carbon-fiber based papers and cloths. The through-plane thermal conductivity of such materials typically ranges between 0.3 and 3 W/m K. In addition, compression (e.g. under the land) will increase the thermal conductivity value by improving the contact between fibers. Graphite is the
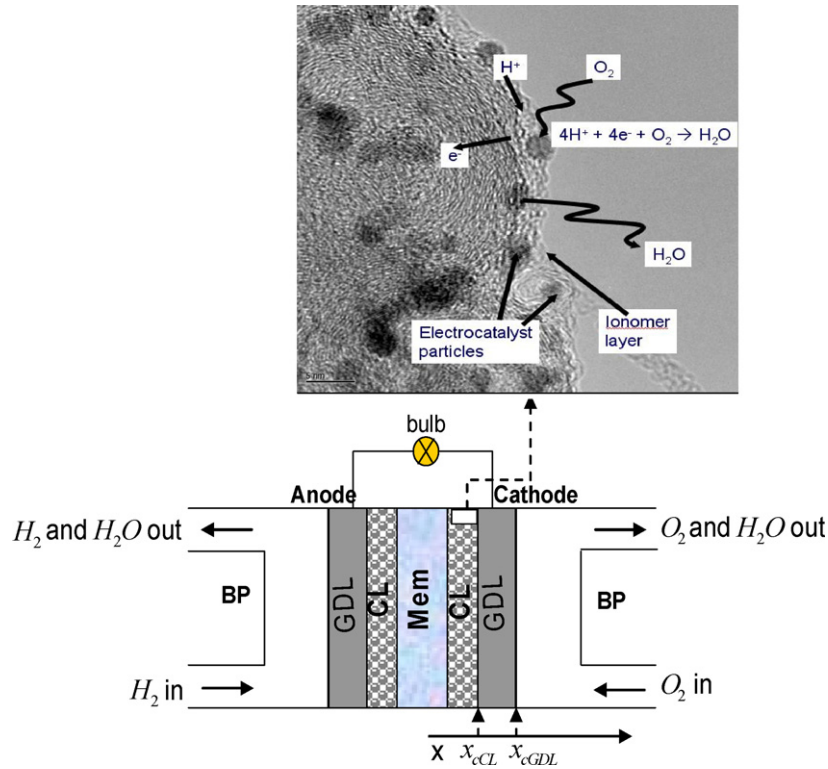
Fig. 1. Schematic of a PEFC and TEM image of the cathode catalyst layer. Water is a product of the oxygen reduction reaction (ORR).

typical bipolar plate material used in PEFCs and with a high thermal conductivity ($\sim$20 W/m K [4]). Some metals, such as stainless steels, are also considered as potential BP materials characterized by a comparable thermal conductivity and excellent elasticity (so they can be made thinner). The temperature variations in these two components ΔT_{GDL} and ΔT_{BP} can also be evaluated from Eq. (1) with the GDL/BP thermal conductivities. Given the range of the relevant parameters, one can obtain ΔT_{GDL} and ΔT_{BP} of <0.3 and 0.05 K, respectively. Note that these variations are small compared to those during cold start ($\sim$10 K), thus the lumped system analysis can be applied.

Considering the fuel cell as a lumped system, the cell temperature evolution is then proportional to the waste heat produced. For constant heat generation, self-heating and negligible heat loss to the surrounding, the time that is required to heat the cell up to 0 °C can be evaluated by using:

$$\tau_{T,1} = \frac{m\bar{c}_p}{I(E_o - V_{cell})A_m}(273.15 - T_o) \tag{2}$$

where m is the mass of the fuel cell, $\bar{c}_p$ the average specific heat, and A_m the reaction area. For evaluation purposes, the thermal mass of
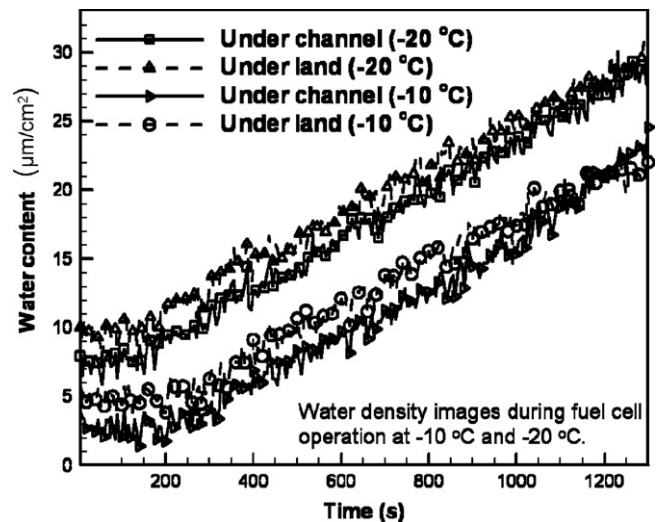

Fig. 2. The water content evolutions from the neutron images during fuel cell operation at two subfreezing temperature −10 and −20 °C.

Table 1
Geometrical, physical, and operating parameters.

| Components	Value
Catalyst layer/GDL/BP thickness, $\delta_{CL}/\delta_{GDL}/\delta_{BP}$	0.01/0.2/1.0 mm
Porosity of GDLs/catalyst layers, $\varepsilon_{GDL}/\varepsilon_{CL}$	0.6/0.5
Volume fraction of ionomer in catalyst layers, ε_m	0.2
Activation energy for oxygen reduction reaction, E_a	73269 J/mol
Thermal conductivity of catalyst layer/GDL/BP, $k_{CL}^{eff}/k_{GDL}^{eff}/k_{BP}^{eff}$	0.3–3.0/0.28–3.0/20 W/m K
Density of ice/dry membrane, ρ_{ice}/ρ_m	917/1980 kg/m³
O₂ diffusivity in cathode gas at standard condition, $D_{M,0}^{O_2}$	3.24×10^{-5} m²/s
Net water transport per proton, α	0.1
Transfer coefficient, α_c	1.0
Exchange current density × reaction surface area, $a_0 i_0^c$	10000.0 A/m³
EW (equivalent weight)	1.1
Latent heat of ice fusion, h_{fusion}	3.34×10^5 J/kg
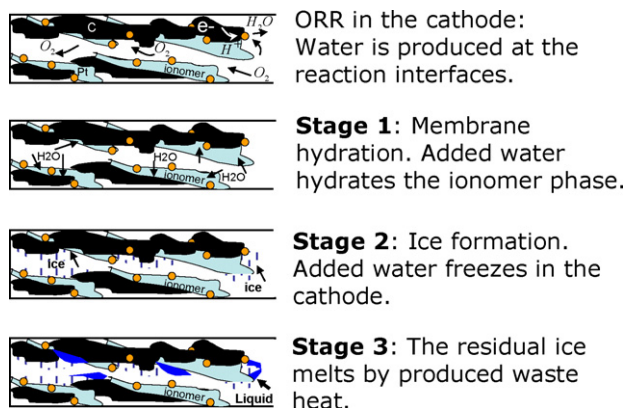
Fig. 3. The three stages of fuel cell cold start.

the bipolar plates (BP) can be considered to dominate. Note that the BP thermal mass depends upon the material properties and the thickness. In addition, in practice coolant channels are embedded in the bipolar plate. Coolant flow could facilitate heat transfer from an external source to improve fuel cell cold start. In the case of self-heating, which is considered in this paper, coolant either remains stagnant in the fuel cell or is drained out during the cold start. In the former case, the residual coolant will contribute to the heat capacity, which may be comparable with that of the bipolar plate. For simplicity in this analysis, we assume that the coolant is drained out during cold start. For the material of choice, e.g. graphite, $\rho_{BP}c_{p,BP}$ of $\sim$1600 kJ/K m^3. δ_{BP} of $\sim$2 mm yields $\tau_{T,1}$ of $\sim$100 s for cold start at $-30\,^{\circ}$C @ 0.1 A/cm^2. While for metals such as stainless steel (e.g. 316 grade), $\rho_{BP}c_{p,BP}$ is $\sim$4000 kJ/K m^3 which leads to $\tau_{T,1}$ of $\sim$300 s for a similar BP thickness. In some cases, the cold start current may be as low as 0.04 A/cm^2 and $\tau_{T,1}$ then nearly doubles to over 10 min for the stainless steel BP. Note that the stainless steel BP can be fabricated thinner, for δ_{BP} of $\sim$0.5 mm $\tau_{T,1}$ may decrease to half of the graphite one.

In addition, the assumption of constant heat generation rate is a good approximation for constant current operation during cold start. This is due to the small cell voltage variation until the fast drop of cell voltage arising from the mass transport polarization (which typically takes place in a short time period) [19]. Under this assumption, the temperature evolution can be estimated by

$$T = \frac{t}{\tau_{T,1}}(273.15 - T_o) + T_o \tag{3}$$

2.2. Stages of cold start process

In the cathode catalyst layer, the net water change rate equals the sum of the production rate due to ORR and that transported through the boundaries. Water in the cathode may exist in the ionomer, gaseous, and ice phases at subfreezing condition (assuming no super cooled liquid exists). Assuming equilibrium among water in the phases prevails due to the small dimension of the pores ($\sim$0.1 μm), solid water emerges after the gaseous phase reaches saturation. Therefore, the first stage of the cold start is water accumulation in the ionomer and gas phases till the saturation vapor pressure limit is reached. In the second stage, the ionomer and gaseous phases are saturated, and water is added to the solid phase, therefore this stage is characterized by ice volume growth within the catalyst layer. The third stage starts when the fuel cell reaches 0 $^{\circ}$C, leading to melting of the residual ice in the catalyst layer due to fuel cell heat generation, see Fig. 3.

For analysis purposes, we consider constant current operation during cold start in the following discussion. A constant net water transfer coefficient, α, and heat generation rate are also assumed.

The first stage: In the ionomer phase, water molecules are associated with the sulfonic acid groups. The ionomer is able to hold a large amount of water compared to that in the gaseous phase [2]. Water added to the cathode may be from the water production by the ORR and water osmosis from the anode and membrane. The location of added water is still unclear: Ref. [19] indicates that the amount of water removed by the channel flow is negligible. Considering instantaneous freezing of water and no transport mechanism for solid water, the catalyst layer may be the place that holds most added water [19]. The Las Alamos National Laboratory (LANL) also indicates that solid water may exist in the GDL; one reason may be the transport of supercooled liquid water [31]. Assuming no liquid exists at the supercooled state, the time constant $\tau_{ice,1}$ for the first stage can be estimated by excluding the water accumulation in the gas phase in the catalyst layer [19]:

$$\tau_{ice,1} = \frac{2F\rho_m\varepsilon_m\delta_{CL}(14 - \lambda_0)}{EW(1 + 2\alpha)I} \tag{4}$$

In general, the membrane ionomer density and EW vary negligibly, but the ionomer volumetric content in the electrode may range from 0.13 to 0.4, leading to $\tau_{ice,1}$ of $\sim$0–30 s with δ_{CL} of 10 μm, α of 0.1, and I of 0.1 A/cm^2. Refs. [32–35] discussed the impact of ionomer content on the electrode performance at standard conditions. At this stage, product water is added to the ionomer phase, increasing the hydration level of the cathode and hence the ionic conductivity. Our experimental data provide evidence of such an initial period of a decreasing HFR, see Fig. 4. The decreasing duration ($\sim$150 s) is at the same magnitude of the time constant calculated through Eq. (4) for 0.02 A/cm^2.

Note that in the above we consider an overall water loss of the anode and membrane to the cathode due to the electro-osmotic drag, i.e. a positive net water transfer coefficient α (=0.1 in our case). In the transient case, α may be a function of time as discussed in Ref. [19]. It characterizes the net water flux due to the water electro-osmotic drag and water back-diffusion. At subfreezing temperature, water diffusivity in the membrane becomes low, which may result in a net water flow to the cathode. This phenomenon can be qualitatively verified through our isothermal cold start experiment, see Fig. 4. Fig. 4 shows the HFR (high frequency resistance) evolutions during cold start from -10 and $-20\,^{\circ}$C, respectively. Initially the HFR decreases which may due to the net water addition in the cathode ionomer phase from water production. After the cathode ionomer is saturated (i.e. the second stage), the water addition is to the solid phase instead of to the ionomer phase, while the anode and membrane keep losing water to the cathode, which
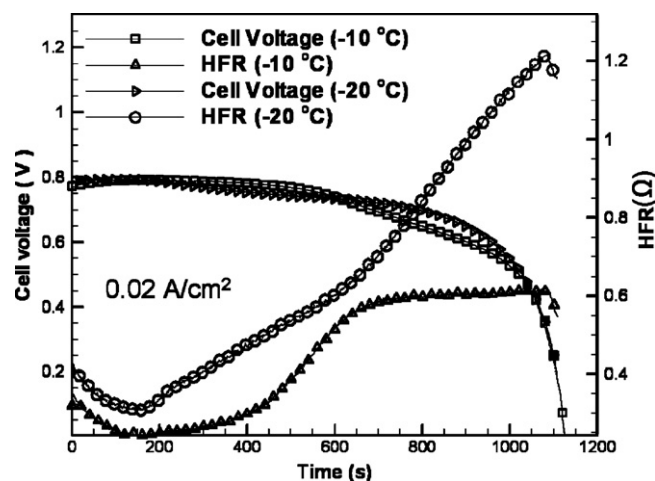

Fig. 4. The HFR (high frequency resistance) and cell voltage evolutions during fuel cell operation at two subfreezing temperature -10 and $-20\,^{\circ}$C.

increases the HFR as indicated in Fig. 4. Details of the experiments regarding Figs. 2 and 4 can be found in Ref. [36].

The second stage: Assuming no liquid water exists at super cooled state, solid water will emerge at $t > \tau_{ice,1}$ and its production rate is proportional to the water addition rate on the cathode side. Considering all the water addition is in the cathode catalyst layer, the ice volume fraction in the void space, s_{ice}, can be expressed as follows:

$$s_{ice}(t) = \frac{t}{\tau_{ice,2}} - k_\tau \quad \tau_{ice,1} < t \leq \tau_{ice,2} + \tau_{ice,1} \tag{5}$$

where $\tau_{ice,2}$ and k_τ are defined as follows:

$$\tau_{ice,2} = \frac{2F\varepsilon_{CL}\rho_{ice}\delta_{CL}}{(1+2\alpha)M^w I} \quad \text{and} \quad k_\tau = \frac{\tau_{ice,1}}{\tau_{ice,2}} = \frac{\rho_m \varepsilon_m (14-\lambda_0)M^w}{\rho_{ice}\varepsilon_{CL}EW} \tag{6}$$

Note that k_τ is the ratio of the two time constants and determined by the composition and material properties as well as initial membrane condition. Given the typical values of these parameters, the ratio ranges from 0 to 0.35.

The time constant $\tau_{ice,2}$ relates the ice accumulation capacity of the catalyst layer to the solid water production rate. Considering the ranges of the parameters as shown in Table 1, $\tau_{ice,2}$ is around 50–150 s at 0.1 A/cm^2. Note that $\tau_{s_{ice}}$, the sum of $\tau_{ice,2}$ and $\tau_{ice,1}$, represents the time that ice fully occupies the open pores in the catalyst layer (i.e. $s_{ice} = 1$). A dimensionless parameter β_2 can be defined based on our earlier work [19] as the ratio of the time constants for ice formation and temperature increase and can be expressed by

$$\beta_2 = \frac{\tau_{T,1}}{\tau_{s_{ice}}} = \frac{(273.15 - T_o)(1+2\alpha)\bar{c}_p}{2F(E_o - V_{cell})}$$
$$\times \frac{1}{(\rho_m \varepsilon_m (14-\lambda_0))/(\rho_{BP}EW) + (\varepsilon_{CL}\rho_{ice})/(M^w \rho_{BP})} \frac{\delta_{BP}}{\delta_{CL}} \tag{7}$$

In the above, we assume the thermal mass of the fuel cell approximates that of the bipolar plate (BP), i.e. $m\bar{c}_p/A = \rho_{BP}\bar{c}_p\delta_{BP}$. At $\beta_2 < 1$, the fuel cell can start up successfully, otherwise, it will fail due to ice build-up. The above equation also indicates selection of the bipolar plate material (e.g. ρ_{BP} and $\bar{c}_p$) and the ratio of BP thickness to that of the catalyst layer affect fuel cell cold start characteristics. For the case of $\beta_2 < 1$, the maximum average of the ice volume fraction s_{ice}^{max} in the catalyst layer can be estimated by

$$s_{ice}^{max} = \frac{\tau_{T,1}}{\tau_{ice,2}} - k_\tau \tag{8}$$

Note that even though physically s_{ice}^{max} must not be over 1, the expression of Eq. (8) can mathematically be extended to the case of $\beta_2 > 1$. In that case, similar to β_2, Eq. (8) can be used as another criterion to evaluate the cold start operation. At $s_{ice}^{max} > 1$, the cold start will fail.

The third stage: For $\beta_2 > 1$, the PEFC will encounter the third stage of cold start, i.e. ice melting. This stage is characterized by a constant cell temperature of 0 °C. The characteristic time scale $\tau_{T,2}$ can be estimated by comparing the heat generation rate with the ice melting latent heat:

$$\tau_{T,2} = \frac{\rho_{ice}h_{fusion}\delta_{CL}\varepsilon_{CL}}{I(E_o' - V_{cell})}s_{ice}^{max} \tag{9}$$

Here E_o' is defined for the condition with liquid water at 0 °C as product. The ratio of $\tau_{T,2}$ to $\tau_{ice,2}$ is then expressed as follows:

$$\frac{\tau_{T,2}}{\tau_{ice,2}} = \frac{h_{fusion}(1+2\alpha)M^w}{2F(E_o' - V_{cell})}s_{ice}^{max} \tag{10}$$

Note that the electrode properties and current vanish in the above equation. The ratio varies from 0 to 0.04, indicating that the third

region is short. During this third stage, the ice volume fraction can be expressed as follows:

$$s_{ice} = \left(\frac{\tau_{T,1}}{\tau_{ice,2}} - k_\tau \right) \frac{\tau_{T,2} + \tau_{T,1} - t}{\tau_{T,2}} \quad \tau_{T,1} < t \leq \tau_{T,1} + \tau_{T,2} \tag{11}$$

2.3. The pseudo one-dimensional analysis

For single-layer electrodes or homogenous electrodes, the spatial variation of the reaction rate across the catalyst layer is almost uniform at small $\hbar$ s [32], which is satisfied for most cold start operation. $\hbar$ is the non-uniformity factor that quantifies the degree of the reaction spatial variation across the cathode electrode ($\hbar = \Delta U/(2(RT/\alpha_c F))$ where $\Delta U = I\delta/\sigma_m^{eff} = IR_\delta$). However, when oxygen transport becomes a limiting factor due to solid water presence, the local reaction rate will vary in the electrode. At high $\hbar s$ (e.g. large current densities), even without solid water the reaction current will differ spatially. During cold start, the reaction rate in the cathode can be expressed as [19]:

$$j = -a_0 i_{0,c}^{ref}(1 - s_{ice})^{\tau_a} \exp$$
$$\left[-\frac{E_a}{R}\left(\frac{1}{T} - \frac{1}{353.15} \right) \right] \frac{C^{O_2}}{C^{O_2,ref}} \exp\left(-\frac{\alpha_c F}{RT} \cdot \eta \right) \tag{12}$$

The surface overpotential η is defined as follows:

$$\eta = \Phi_s - \Phi_e - U_o \tag{13}$$

where Φ_s and Φ_e are the electronic and electrolyte phase potentials, respectively.

Eq. (12) directly shows that the reaction rate is a function of the local ice volume fraction as well as the local oxygen concentration. Note that the temperature spatial variation is negligible as estimated previously. Both local ice volume fraction and oxygen concentration may vary spatially due to the local reaction and oxygen/water transport within the cathode. Therefore, in order to obtain the local reaction rate, solving the coupled oxygen/water transport equations and electrochemical kinetics Eq. (12) is a must. A simplified treatment is to consider a constant reaction rate in the electrode and hence a uniform ice formation. Note that this assumption considers the catalyst layer as a number of separated small reactors in the through-plane direction. The reactors are operated at a constant reaction rate, allowing the surface overpotentials to adjust according to the local oxygen content and ice volume fraction. This treatment greatly simplifies the model and enables the impact of ice on electrode performance to be directly evaluated through temporal and spatial variations of the surface overpotential. We herein term this technique the pseudo-1D analysis. The uniform local transfer current and oxygen consumption rate can be expressed as follows:

$$j = -\frac{I}{\delta_{CL}} \quad \text{and} \quad S_{O_2} = -\frac{I}{4F\delta_{CL}} \tag{14}$$

In addition, in the following analysis, we only consider the second stage of cold start when ice starts to form in the cathode. Following the analysis of Ref. [19], the oxygen profile can be obtained:

$$\frac{C^{O_2}}{C_{cCL}^{O_2}} = 1 - Da\frac{1 - \bar{x}^2}{\varepsilon_{CL}^{\tau_d - \tau_{d,0}}[(1 - s_{ice})]^{\tau_d}} \quad \text{where} \quad \bar{x} = 1 - \frac{x_{cCL} - x}{\delta_{CL}} \tag{15}$$

where $\bar{x}$ is the dimensionless distance from the interface between the membrane and catalyst layer, and the dimensionless parameter, Da, is called the Damköhler number. Detailed discussion on Da can be found in Ref. [19]. In addition, severe local oxygen starvation will first occur at $\bar{x} = 0$ when $C^{O_2} = 0$, i.e.:

$$1 = Da\frac{1}{\varepsilon_{CL}^{\tau_d - \tau_{d,0}}[(1 - s_{ice}^{starvation})]^{\tau_d}} \tag{16}$$

Assuming $\tau_d = \tau_{d,0}$, the above equation can be simplified as follows:

$$s_{ice}^{starvation} = 1 - \sqrt[\tau_d]{Da} \tag{17}$$

For $\tau_d = 2$ and $Da \sim 1.0 \times 10^{-4}$, $s_{ice}^{starvation} \sim 99\%$. Note that τ_d plays a critical role in determining the value of $s_{ice}^{starvation}$.

The oxygen profile in the catalyst layer of Eq. (15) can be substituted to Eq. (12), yielding:

$$\eta(s_{ice}, \bar{x})$$

$$= -\frac{RT}{\alpha_c F} \ln \left\{ \frac{IC_{O_2,ref}}{a_0 i_{0,c}^{ref} \exp\left[-\frac{E_a}{R}\left(\frac{1}{T_o} - \frac{1}{353.15}\right)\right] C_{cCL}^{O_2} \delta_{CL}} \exp\left[\frac{E_a}{R}\left(\frac{1}{T} - \frac{1}{T_o}\right)\right] \right\}$$

$$+ \frac{RT}{\alpha_c F} \ln \left[(1 - s_{ice})^{\tau_a} \left(1 - Da \frac{1 - \bar{x}^2}{\varepsilon_{CL}^{\tau_d - \tau_{d,0}}(1 - s_{ice})^{\tau_d}}\right)\right] \tag{18}$$

Note that the impacts of ice are all included in the second term on the right while the first primarily accounts for the temperature dependence of the exchange current density. The overpotential can further be written as follows:

$$\eta(s_{ice}, T, \bar{x}) = -\frac{RT}{\alpha_c F} \ln \left(\frac{IC^{O_2,ref}}{a_0 i_{0,c}^{ref} \exp\left[-\frac{E_a}{R}\left(\frac{1}{T_o} - \frac{1}{353.15}\right)\right] C_{cCL}^{O_2} \delta_{CL}} \right)$$

$$- \frac{T E_a}{\alpha_c F}\left(\frac{1}{T} - \frac{1}{T_o}\right) + \frac{RT \tau_a}{\alpha_c F} \ln(1 - s_{ice})$$

$$+ \frac{RT}{\alpha_c F} \ln \left(1 - Da \frac{1 - \bar{x}^2}{\varepsilon_{CL}^{\tau_d - \tau_{d,0}}(1 - s_{ice})^{\tau_d}}\right)$$

$$= \eta_o + \Delta\eta_T + \Delta\eta_{c,1} + \Delta\eta_{c,2} \tag{19}$$

where

$$\eta_o = -\frac{RT}{\alpha_c F} \ln \left(\frac{IC^{O_2,ref}}{a_0 i_{0,c}^{ref} \exp\left[-\frac{E_a}{R}\left(\frac{1}{T_o} - \frac{1}{353.15}\right)\right] C_{cCL}^{O_2} \delta_{CL}} \right),$$

$$\Delta\eta_T = -\frac{T E_a}{\alpha_c F}\left(\frac{1}{T} - \frac{1}{T_o}\right), \quad \Delta\eta_{c,1} = \frac{RT \tau_a}{\alpha_c F} \ln(1 - s_{ice}) \quad \text{and}$$

$$\Delta\eta_{c,2} = \frac{RT}{\alpha_c F} \ln \left(1 - Da \frac{1 - \bar{x}^2}{\varepsilon_{CL}^{\tau_d - \tau_{d,0}}(1 - s_{ice})^{\tau_d}}\right) \tag{20}$$

Physically, η_o denotes the overpotential at the interface between the cathode catalyst layer and GDL at T_o when no ice is present, while $\Delta\eta_T$ represents the overpotential variation due to dependence of the exchange current on temperature. $\Delta\eta_{c,1}$ and $\Delta\eta_{c,2}$ arise from the ice presence in the catalyst layer and are defined following Ref. [19] which conducted an extensive discussion on these two overpotential changes and their ratio $\beta_3 = \Delta\eta_{c,1}/\Delta\eta_{c,2}$, and the voltage drops observed in Fig. 4, which considers isothermal subfreezing operation, are primarily due to these two mechanisms of the voltage loss. Note that the Tafel slope $-(RT/\alpha_c F)$ also contains temperature. In general, the dependence of the Tafel slope on temperature is not the dominant mechanism, rather the one of the exchange current density is more important for the electrochemical kinetics. Also, there has been extensive discussion on the temperature dependence of the Tafel slope. Some claim [37,38] that the Tafel slope is temperature invariant for the oxygen reduction reaction in certain cases due to fact that the transfer coefficient α_c may be temperature-dependent [39]. Ref. [40] discussed several possible mechanisms that contribute to the temperature dependence of the transfer coefficient. Therefore, in expression of $\Delta\eta_T$ we can treat T/α_c as a constant. The maximum value, $\Delta\eta_T^{max}$, during cold start can be calculated by $-(T_o E_a/\alpha_c F)((1/273.15) - (1/T_o))$.

2.4. Temperature dependence of the ohmic polarization

Temperature can affect the ionic conductivity and therefore the ohmic voltage loss ($\Delta V_{ohm} = R_\Omega I$). The ohmic resistance due to proton transport $R_\Omega^{H^+}$ can be expressed by [19]:

$$R_\Omega^{H^+} = \frac{\delta_m}{\sigma_m} + \frac{\delta_{aCL}}{2\sigma_m^{aCL,eff}} + \frac{\delta_{cCL}}{2\sigma_m^{cCL,eff}} \tag{21}$$

The above ionic conductivities σ_m, $\sigma_m^{aCL,eff}$, and $\sigma_m^{cCL,eff}$ are the averages over the membrane, anode and cathode catalyst layers, respectively. The latter two can be calculated by considering the Bruggeman correlation:

$$\sigma_m^{aCL,eff} = \varepsilon_m^{1.5} \sigma_m^{aCL} \quad \text{and} \quad \sigma_m^{cCL,eff} = \varepsilon_m^{1.5} \sigma_m^{cCL} \tag{22}$$

The ionic conductivity σ_m is a function of the local water content and temperature, as indicated by Springer et al. [41] for standard (above-zero) operating condition. At subfreezing temperature, part of the water in the membrane may freeze and affect the ionic conductivity. Our previous experiment [42] measured the ionic conductivity of Nafion® 117 from −30 to 0 °C. The fitted ionic conductivity expression (considering a similar form as Springer et al. [41]) is as follow and shown in Fig. 5, together with the experimental data:

$$\sigma_m = (0.01862\lambda - 0.02854) \exp\left[4029\left(\frac{1}{303} - \frac{1}{T}\right)\right] \quad \text{or}$$

$$= (0.004320\lambda - 0.006620) \exp\left[4029\left(\frac{1}{273} - \frac{1}{T}\right)\right]$$

$$= \sigma_{m,0}(\lambda) \exp\left[4029\left(\frac{1}{273} - \frac{1}{T}\right)\right] \quad \text{for} \quad \lambda \leq 7.22$$

$$\sigma_m = \sigma_m(\lambda = 7.22) \quad \text{for} \quad \lambda > 7.22 \tag{23}$$

It can be seen that the ionic conductivity above $\lambda > 7.22$ (the water activity, $a > 80\%$) shows a complex pattern of changing with the water content λ, which may due to the fact that part of water in the ionomer phase freezes. Note that a higher water content may reduce the portion of nonfreezing water through interacting with the sulfonic groups. More discussions on the ionic conductivity for $\lambda > 7.22$ can be found in our previous work [42]. For model-
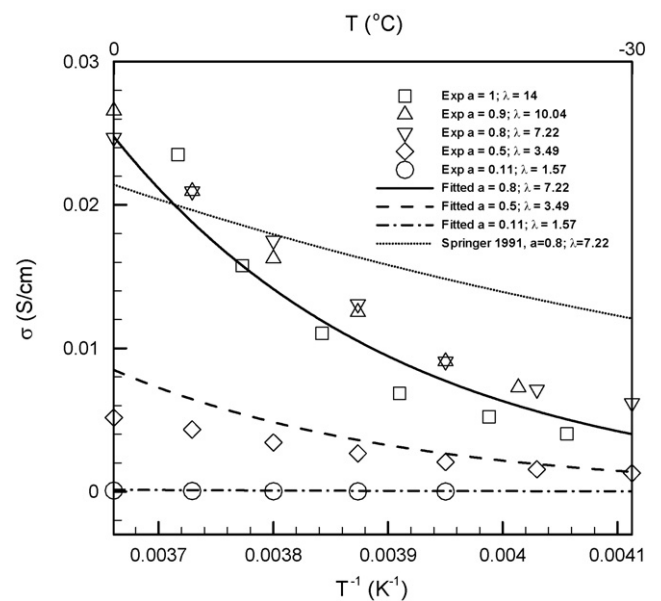

Fig. 5. The dependence of the ionic conductivity on temperature and water content, and comparison of the fitting curve of Eq. (23) and experimental data based on the Nafion® 117.

ing/simulation purposes, Eq. (23) assumes the ionic conductivity is independent of λ for $\lambda > 7.22$:

$$\Delta V_{\text{ohm}}^{\text{H}^+} = R_{\Omega}^{\text{H}^+} I$$

$$= \left(\frac{\delta_m}{\sigma_{m,0}(\lambda^m)} + \frac{\delta_{a\text{CL}}}{2\sigma_{m,0}(\lambda^{a\text{CL}})\varepsilon_m^{1.5}} + \frac{\delta_{c\text{CL}}}{2\sigma_{m,0}(\lambda^{c\text{CL}})\varepsilon_m^{1.5}} \right) \exp$$

$$\times \left[-4029 \left(\frac{1}{273} - \frac{1}{T} \right) \right] I$$

$$= R_{\Omega,273\,\text{K}}^{\text{H}^+}(\bar{\lambda}) \exp \left[-4029 \left(\frac{1}{273} - \frac{1}{T} \right) \right] I \tag{24}$$

where $\bar{\lambda}$ is average over the whole MEA. To assess the temperature impact, one can differentiate the above equation and consider a temperature change of dT:

$$d(\Delta V_{\text{ohm}}^{\text{H}^+}) = \left[\frac{dR_{\Omega,273\,\text{K}}^{\text{H}^+}}{d\lambda} \exp \left[-4029 \left(\frac{1}{273} - \frac{1}{T} \right) \right] d\lambda \right.$$

$$\left. - \frac{4029}{T^2} R_{\Omega,273\,\text{K}}^{\text{H}^+} \exp \left[-4029 \left(\frac{1}{273} - \frac{1}{T} \right) \right] dT \right] I \tag{25}$$

Note that if the hydration level of the MEA is always above 7.22, the first term in the bracket is zero. The second one can be used to estimate the magnitude of the ohmic voltage loss variation by integrating from T to $T + dT$. Considering $\lambda = 14$, $T = -30\,^\circ\text{C}$ and $dT = 30\,^\circ\text{C}$ as well as other parameters in Table 1, the value of $R_{\Omega,273\,\text{K}}^{\text{H}^+}$ is $\sim 700\,\text{m}\Omega\,\text{cm}^2$, which renders $d(\Delta V_{\text{ohm}}^{\text{H}^+})| \sim 0.18\,\text{V}$ @ $0.1\,\text{A/cm}^2$. Note that the calculated $d(\Delta V_{\text{ohm}}^{\text{H}^+})|_{-30\,^\circ\text{C}}^{0\,^\circ\text{C}}$ is much higher than $\Delta\eta_T^{\text{max}}$. In addition, using the data of Springer et al. [41], the value of $d(\Delta V_{\text{ohm}}^{\text{H}^+})|_{-30\,^\circ\text{C}}^{0\,^\circ\text{C}} \sim 0.03\,\text{V}$, which underestimates the degree of temperature dependence of the ohmic polarization.

3. Results and discussion

Fig. 6 shows evolution of the ice volume fraction s_{ice} at different initial membrane water contents λ_0. The three stages of the cold start are shown for the cases of $\lambda_0 = 1$ and 7. For all the cases, $\tau_{T,1}$ is $\sim 50\,\text{s}$ as indicated in Fig. 6. For $\lambda_0 = 13$, s_{ice} reaches 1 before time of $\tau_{T,1}$, demonstrating that the cold start would fail due to ice build-up in the catalyst layer. Purging the fuel cell with dry air upon shut-down is a typical method to improve cold start characteristics, in which the membrane hydration level is reduced to increase
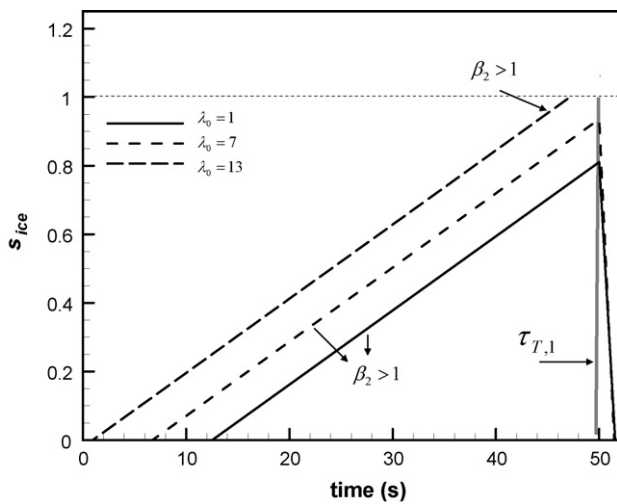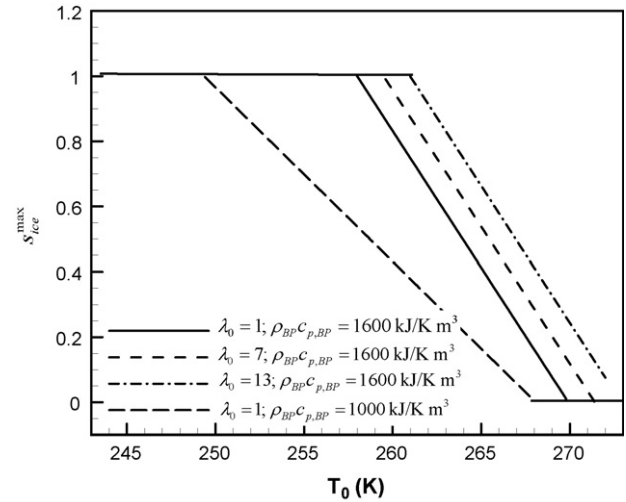

Fig. 7. The theoretical maximum ice volume fraction as a function of cold start temperature and bipolar plate thermal properties.

the time scale of $\tau_{\text{ice},1}$. However, even though the purge technique enhances cold start characteristics, the improvement is not significant when the time scale of the first stage of cold start $\tau_{\text{ice},1}$ is much smaller than the second one, (see k_τ which indicates the ratio of the two time constants and is evaluated around 0–0.35). Further, the third stage is short as shown for the cases of $\lambda_0 = 1$ and 7, which is consistent with the preceding analysis, i.e. $(\tau_{T,2}/\tau_{\text{ice},2}) \sim 0 - 0.04$.

Fig. 7 displays the theoretical maximum ice volume fraction $s_{\text{ice}}^{\text{max}}$ within the cathode catalyst layer as a function of cold start temperature T_0. For the cases with the graphite bipolar plate, i.e. $\rho_{\text{BP}} c_{p,\text{BP}} = 1600\,\text{kJ/K}\,\text{m}^3$, it shows that $s_{\text{ice}}^{\text{max}}$ increases as the cold start temperature is reduced. The temperature regime where $s_{\text{ice}}^{\text{max}}$ reaches 1 corresponds to a failed cold start. In addition, it also shows reducing the initial λ_0 (e.g. the gas purge) has limited impact on cold start characteristics, particularly to that with different bipolar plate materials. Further, for the fuel cell with the considered bipolar plates, self-cold starts above $-10\,^\circ\text{C}$ are likely successful as $s_{\text{ice}}^{\text{max}}$ is less than 1.
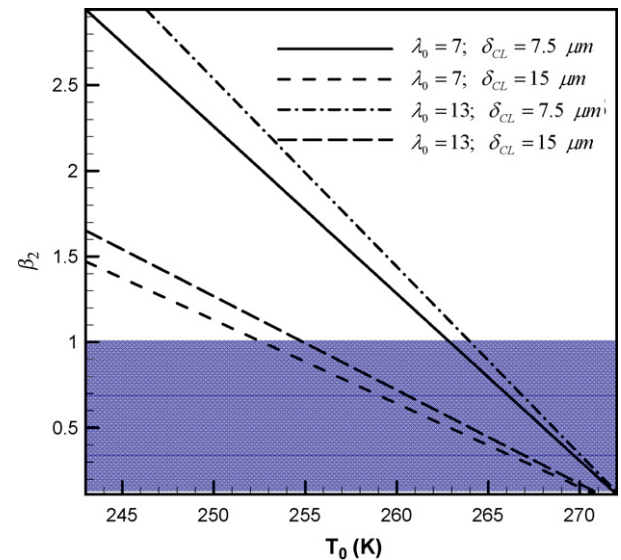

Fig. 6. The ice volume fraction vs. time at constant current density of $0.1\,\text{A/cm}^2$.

Fig. 8. Profiles of β_2 as a function of cold start temperature at different initial λ_0s and cathode catalyst layer thicknesses.
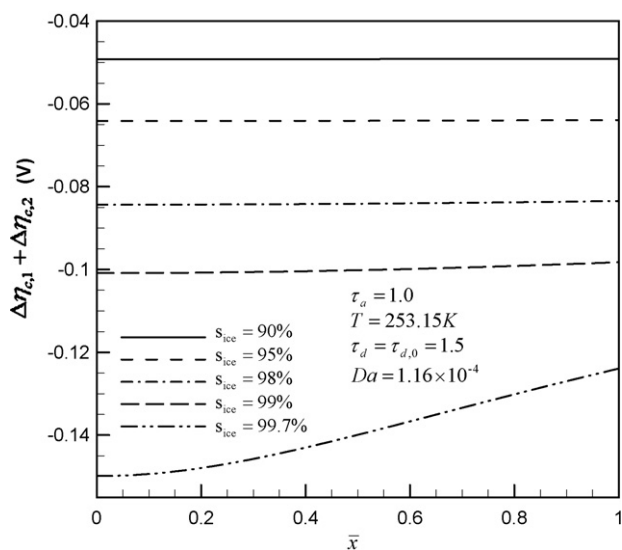
Fig. 9. Profiles of $\Delta\eta_{c,1} + \Delta\eta_{c,2}$ across the cathode catalyst layer for different ice volume fractions.

Fig. 10. Comparison of the magnitudes of $\Delta\eta_T^{max}$ and $\Delta\eta_{c,1}$.

Fig. 8 presents the profiles of β_2 as a function of cold start temperature at different initial water contents λ_0 and catalyst layer thicknesses. As discussed previously, β_2 is another key parameter defined in Ref. [19] that characterizes the cold start operation. In the gray region that $\beta_2 < 1$, the cold start can succeed, while it fails in the area above. In addition, similar to the previous figure, β_2 increases with decreasing initial cold start temperatures. Reducing λ_0 shows a small improvement on cold start characteristics compared to the change in fuel cell design, i.e. increasing the catalyst layer thickness as shown in Fig. 8.

Fig. 9 displays the profiles of the sum of the two overpotential variations related to solid water, $\Delta\eta_{c,1} + \Delta\eta_{c,2}$, across the cathode catalyst layer for different ice volume fractions. Between the two components in the plotted overpotential variation, only the second overpotential variation is dependent on location while the first one is solely a function of the local ice volume fraction. Consistent with the discussion in Ref. [19], the local oxygen transport polarization starts to become important at the high ice volume fraction, i.e. $s_{ice} = 99.7\%$. Even at $s_{ice} = 99\%$, the variation is still small and not evident. Further, the potential drop with s_{ice} primarily results from the first term in most range of the cold start, i.e. the mechanism of the ice coverage over the active reaction surface, which has been extensively discussed in Ref. [19].

Fig. 10 compares the magnitudes of $\Delta\eta_T^{max}$ and $\Delta\eta_{c,1}$. $\Delta\eta_{c,1}$ characterizes the impact of the ice coverage over the electrochemical reaction surface, and increases in magnitude quickly with s_{ice} as shown in Fig. 10. Note that the ice coverage just temporarily blocks the oxygen access to the active reaction site, while the disabled interface, still accessible to electrons and protons, is generally able to recover after the solid water is removed. The figure shows that temperature has little impact on the value of $\Delta\eta_{c,1}$, instead the influence of the coefficient τ_α is evident. Further, the magnitudes of $\Delta\eta_T^{max}$ are also indicated in Fig. 10. Two values of the activation energy are considered [37]. Note that these values are according to different Tafel slopes with the higher value 73.3 kJ/mol corresponding to -60 mV/decade or low-current-density region while the other to -120 mV/decade or high-current-density region. The values of $\Delta\eta_T^{max}$ plotted in the figure exclude the temperature-difference of the Tafel slope. Therefore the value primarily gives the magnitude of the overpotential change due to the temperature dependence of exchange current density. From this figure, it can be seen that $\Delta\eta_{c,1}$ is comparable with $\Delta\eta_T$ at low and intermediate ice volume fraction regions, while $\Delta\eta_{c,1}$ dominates at the high
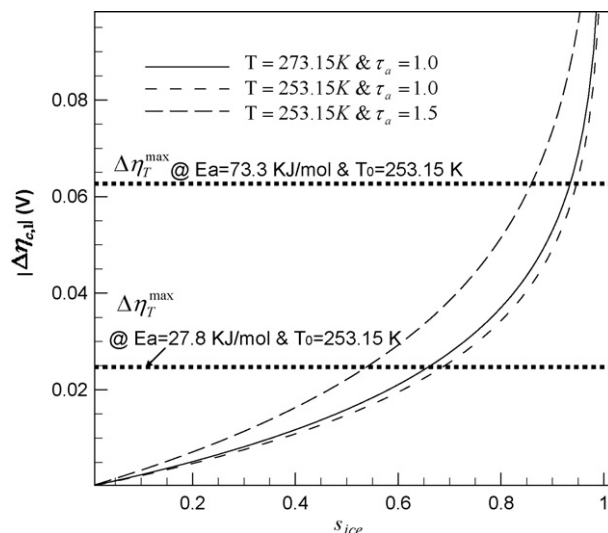
fraction of s_{ice}. At $s_{ice} > 95\%$, the adverse impact of the solid water will lead to a fast drop of the cell voltage that has been observed in most studies [19,22].

4. Conclusions

In this paper, a theoretical study is presented on the electrochemical and transport phenomena in the cathode catalyst layer of fuel cells for cold start operation. The spatial variations of temperature within fuel cell components were evaluated. A lumped system analysis was performed to investigate the characteristics of cell temperature evolution and ice volume fraction within fuel cells. Through examining the time scales for temperature and solid water evolution, three stages of cold start were identified and investigated. Gas purge can enhance cell cold start characteristics but the improvement potential is limited compared to other methods such as materials property modification and cell design optimization. Further, pseudo-1D analysis was developed and spatial variations of the oxygen concentration and overpotential were investigated. Oxygen transport limitation was found to occur at high ice volume fraction regions, especially in CL with high tortuosities. In addition, we decoupled the impacts from the temperature variation, ice coverage over the electrochemical reaction surface, and oxygen transport limitation during the cold start and compared their magnitudes. The temperature dependence of the ohmic polarization during cold start was estimated based on the ionic conductivity of the Nafion membrane at subfreezing temperature.

References

[1] C.Y. Wang, Chem. Rev. 104 (2004) 4727.
[2] Y. Wang, C.Y. Wang, Electrochim. Acta 50 (2005) 1307.
[3] R. Madhusudana Rao, R. Rengaswamy, Chem. Eng. Sci. 61 (2006) 7393–7409.
[4] Y. Wang, C.Y. Wang, Electrochim. Acta 51 (2006) 3924.
[5] Y. Wang, C.Y. Wang, J. Electrochem. Soc. 154 (2007) B636–643.
[6] G. Hu, J. Fan, J. Power Sources 165 (2007) 171–184.
[7] A.A. Shah, G.-S. Kim, P.C. Sui, D. Harvey, J. Power Sources 163 (2007) 793–806.
[8] H. Meng, J. Power Sources 171 (2) (2007) 738–746.
[9] S.-M. Chang, H.-S. Chu, J. Power Sources 172 (2) (2007) 790–798.
[10] A.A. Shah, P.C. Sui, G.-S. Kim, S. Ye, J. Power Sources 166 (2007) 1–21.
[11] Y. Shan, S.-Y. Choe, S.-H. Choi, J. Power Sources 165 (2007) 196–209.
[12] Y. Hishinuma, T. Chikahisa, F. Kagami, T. Ogawa, JSME Int. J., Ser. B 47 (2004) 235.
[13] M.S. Wilson, J.A. Valerio, S. Gottesfeld, Electrochim. Acta 40 (1995) 355.
[14] R.C. McDonald, C.K. Mittelsteadt, E.L. Thompson, Fuel Cells 4 (2004) 208.
[15] E. Cho, J.J. Ko, H.Y. Ha, S.A. Hong, K.Y. Lee, T.W. Lim, I.H. Oh, J. Electrochem. Soc. 151 (2004) A661.

[16] M. Oszcipok, D. Riemann, U. Kronenwett, M. Kreideweis, M. Zedda, J. Power Sources 145 (2005) 407.
[17] Q. Yana, H. Toghianib, Y.-W. Leea, K. Liangb, H. Causey, J. Power Sources 160 (2006) 1242.
[18] R. Mukundan, Y.S. Kim, T. Rockward, J.R. Davey, B.S. Pivovar, D.S. Hussey, D.L. Jacobson, M. Arif, R.L. Borup, ECS Trans. 11 (2007) 543–552.
[19] Y. Wang, J. Electrochem. Soc. 154 (2007) B1041–B1048.
[20] L. Mao, C.Y. Wang, J. Electrochem. Soc. 154 (2007) B341.
[21] F. Jiang, W. Fang, C.-Y. Wang, Electrochim. Acta 53 (2) (2007) 610–621.
[22] H. Meng, Int. J. Hydrogen Energy 33 (2008) 5738–5747.
[23] K. Jiao, X. Li, Electrochim. Acta 54 (27) (2009) 6876–6891.
[24] E.L. Thompson, J. Jorne, W. Gu, H.A. Gasteiger, J. Electrochem. Soc. 155 (2008) B625–B634.
[25] M. Saito, K. Hayamizu, T. Okada, J. Phys. Chem. B 109 (2005) 3112.
[26] M. Cappadonia, J.W. Erning, S.M.S. Niaki, U. Stimming, Solid State Ionics 77 (1995) 65.
[27] W. Song, J. Hou, H. Yu, L. Hao, Z. Shao, B. Yi, Int. J. Hydrogen Energy 33 (2008) 4844–4848.
[28] E.L. Thompson, J. Jorne, H.A. Gasteiger, J. Electrochem. Soc. 154 (2007) B783–B792.
[29] K.L. Moore, K.S. Reeves, DOE Hydrogen Program Annual Merit Review Proceedings, Arlington, VA, USA, May 23–26, 2005.
[30] Y. Wang, C.Y. Wang, J. Electrochem. Soc. 153 (6) (2006) A1193.
[31] Y. Wang, R. Mukundan, R.L. Borup, Private Communication, 2008.
[32] Y. Wang, X. Feng, J. Electrochem. Soc. 155 (12) (2008) B1289–B1295.
[33] E. Antolini, L. Giorgi, A. Pozio, E. Passalacqua, J. Power Sources 77 (1999) 136–142.
[34] R. Madhusudana Rao, R. Rengaswamy, Trans IChemE. Part A: Chem. Eng. Res. Des. 84 (A10) (2006) 952–964.
[35] Y. Wang, X. Feng, J. Electrochem. Soc. 156 (3) (2009) B403–B409.
[36] R. Mukundan, J.R. Davey, R.W. Lujan, J.S. Spendelow, Y.S. Kim, D.S. Hussey, D.L. Jacobson, M. Arif, R.L. Borup, ECS Trans. 16 (2) (2008) 1939–1950.
[37] A. Parthasarathy, S. Srinivasan, A.J. Appleby, J. Electrochem. Soc. 139 (1992) 2530.
[38] S.J. Clouser, J.C. Huang, E. Yeager, J. Appl. Electrochem. 23 (1993) 597–605.
[39] B.E. Conway, D.F. Tessier, D.P. Wilkinson, J. Electrochem. Soc. 136 (1989) 2486–2493.
[40] B.E. Conway, in: B.E. Conway, J.O. Bockris, R. White (Eds.), Modern Aspects of Electrochemistry, vol. 16, Plenum, New York, 1986.
[41] T.E. Springer, T.A. Zawodinski, S. Gottesfeld, J. Electrochem. Soc. 138 (1991) 2334–2341.
[42] R. Mukundan, Y. Kim, F. Garzon, B. Pivovar, ECS Trans. 1 (8) (2006) 403–413.